Effects of Ni incorporation on the reactivity and stability of hausmannite (Mn$_3$O$_4$): Environmental implications for Mn, Ni, and As solubility and cycling

Boyoung Song[a], Elizabeth B. Cerkez[b], Evert J. Elzinga[c], Bojeong Kim[a],*

[a] Department of Earth and Environmental Science, Temple University, Philadelphia, PA 19122, United States
[b] Department of Chemistry, Temple University, Philadelphia, PA 19122, United States
[c] Department of Earth and Environmental Sciences, Rutgers University, Newark, NJ 07102, United States

ABSTRACT

Trace metal structural impurities are common in Mn (II/III) oxides, yet their effects on the oxides' reactivity and stability have not been experimentally assessed. The present investigation quantifies such effects for the first time by measuring the extent of mineral dissolution of pristine and Ni-substituted hausmannite (Mn^{II}Mn$_2^{III}$O$_4$) (at 1 and 2 wt% Ni) in 8-h batch reactions at pH 5 with/without arsenite (As(III)). Ni substitution occurred at Mn(III) octahedral sites, causing noticeable structural modification in lattice parameters with a decrease in Jahn-Teller distortion, particularly at 2 wt%. In both acidic and reductive dissolution (with As(III)), the Ni-substituted hausmannite exhibited enhanced Mn release relative to the pristine mineral, with concurrent release of structural Ni increasing with substitution percentage. When As(V) release was normalized by surface area, Ni-substituted hausmannite showed a higher As(III) oxidation percentage than the pristine phase. Further, higher ratios of Mn (II):As(V) were observed in Ni-substituted hausmannite. As K-edge X-ray absorption spectroscopy and attenuated total reflectance-Fourier transform infrared spectroscopy analyses indicated that As(III) oxidation lead to the formation of binuclear bidentate As(V) surface complexes. Enhanced reactivity of Ni-substituted hausmannite may be attributed to lowered mineral stability, which promotes accelerated mineral dissolution and increased structural Mn release, resulting in formation/exposure of highly reactive sites. Thus, structural impurities dictate the properties, reactivity, and stability of the Mn(II/III) oxides, affecting the level of dissolution and the extent of redox reactions, which together impact the fate and cycling of transition metals and metalloids in surface environments.

1. Introduction

Manganese (Mn) oxides are ubiquitous in nature, and found in various geological settings, ranging from mining areas and ore deposits to sediments in freshwater and marine environments (Chapnick et al., 1982; Chukhrov, 2006; Haack and Warren, 2003; Lee and Xu, 2016; Maynard, 2010; Murray et al., 1984; Post, 1999). They are also among the most reactive mineral phases for adsorption and oxidation reactions, playing critical roles in regulating the speciation and distribution of trace metals and metalloids, as well as the cycling of essential nutrients in natural environments (Chapnick et al., 1982; Greene and Madgwick, 1991; Haack and Warren, 2003; Manceau et al., 2007; Maynard, 2010; Mock et al., 2019; Post, 1999; Taylor, 1968; Tebo et al., 2005; Vodyanitskii, 2009; Wang et al., 2019; Wu et al., 2018). In these natural Mn oxides structural impurities are commonly observed (Chao, 1976; Maynard, 2010; Post, 1999). Structural incorporation of Ni has been noted in oceanic Mn nodules

and crusts (Burns, 1993; Manceau et al., 2007; Peacock and Sherman, 2007), and also in terrestrial Mn-containing mineral and rock samples (Taylor et al., 1964; Taylor and McKenzie, 1966). Therefore, knowledge of the effects of metal impurities on the reactivity and stability of Mn oxides is essential to better understand the geochemical behavior of natural Mn oxides and the fate and mobility of associated transition metal(loid)s.

To date, effects of trace metal impurities on Mn oxide reactivity have been examined primarily for birnessite, the most common natural Mn(II/III/IV) oxide. For example, a recent study by Wang et al. (2019) showed that divalent cations (Zn, Mg and Ca) substituted in the birnessite lattice affected the mineral's ability to adsorb and oxidize fulvic acid, and modified its transformation processes to varying degrees. In addition, Zn appeared to influence the kinetics of the mineral's reductive transformation processes by Mn(II), where Zn-coprecipitated birnessite exhibited a faster conversion rate from birnessite into feitknechtite (β-MnOOH), a metastable Mn-(hydr)oxide, than the pristine phase, but slower conversion of

feitknechtite into more stable manganite (γ-MnOOH) due to the lowered Mn(II) concentration (Zhao et al., 2018). In another study, the structural incorporation of Co(III) in birnessite was observed to inhibit the transformation process into todorokite, producing mineral mixtures of phyllomanganates and todorokite-like tectomanganates (Wu et al., 2019). Transition metals that are originally adsorbed on the surface of birnessite have also been shown to become structurally incorporated during the mineralogical transformation of the adsorbent. For instance, Zn(II)-adsorbed birnessite is converted into a Zn-substituted hausmannite (Zn(II)$_{1-x}$Mn(II)$_x$Mn(III)$_2$O$_4$) through reductive transformation by Mn(II) at circumneutral pH (Lefkowitz and Elzinga, 2015). Similarly, the mineralogical transformation of Ni(II)-sorbed birnessite by Mn(II) results in the formation of Ni-substituted feitknechtite (Lefkowitz and Elzinga, 2017).

Despite accumulating evidence for the importance of metal substituents in affecting Mn oxide reactivity and transformation (Elzinga, 2011; Green et al., 2004; Greene and Madgwick, 1991; Lefkowitz et al., 2013; Lefkowitz and Elzinga, 2015; Manceau et al., 1992; Tebo et al., 2005; Vodyanitskii, 2009; Wang et al., 2018), no studies exist for Mn(III) oxides. Of particular importance is hausmannite (Mn^{II}Mn$_2^{III}$O$_4$), which is a common metastable Mn(II/III) oxide found in various geological settings in both bulk and nano-scale mineral phases (Elzinga, 2011; Green et al., 2004; Greene and Madgwick, 1991; Hem, 1978; Lefkowitz et al., 2013; Lefkowitz and Elzinga, 2015; Pardee, 1927; Tebo et al., 2005; Vodyanitskii, 2009; Wang et al., 2015). It is also one of the secondary Mn(III)-containing mineral phases produced upon reductive transformation of birnessite by mild changes in environmental conditions (Lefkowitz et al., 2013). Further, hausmannite is the most widely distributed spinel structured Mn oxide, with Mn(II) occupying the tetrahedral sites, and Mn(III) in the octahedral sites (O'Neill and Navrotsky, 1983; Post, 1999, 1992). These octahedral Mn(III) sites present structural distortions due to the Jahn-Teller effect. In general, minerals with the spinel structure are capable of housing a broad range of chemical substituents (Dong et al., 2013; Hirai et al., 2016; Li et al., 2014). Hausmannite is no exception, and may accommodate structural incorporation of transition metals such as Ni, Co, and Zn, due to the similar radii of the metal substituents to Mn(II/III) and their close geological association (Green et al., 2004; Lefkowitz and Elzinga, 2015; Shacat et al., 2004). In particular, the dissolution reactions of hausmannite has been related to the pronounced release of Ni in natural aquatic systems, such as Lake Vanda and Lake Joyce (Green et al., 2004; Shacat et al., 2004), yet the fate and geochemical reactivity of Ni-containing hausmannite has been rarely investigated.

In the present study we systematically investigated the effects of Ni impurities on the mineral structure and characteristics, as well as the mineral reactivity and stability of hausmannite by using both pristine and Ni-substituted phases. Specifically, we measured the extent and rate of acidic and reductive mineral dissolution at pH 5 with/without arsenite (As(III)), using these as a means of assessing the mineral's reactivity and stability. Ni is redox-inactive, and hence, does not involve with the As(III) oxidation reaction, which allows us to solely detect changes made in the mineral's reactivity and stability by substitution. Furthermore, we employed a combination of techniques including powder X-ray diffraction (PXRD), synchrotron-based X-ray absorption spectroscopy (XAS), and attenuated total reflectance Fourier transform infrared spectroscopy (ATR-FTIR) for mineral solids characterization before and after batch reactions and to study the reaction in situ. Based on these complementary measurements, we demonstrate that Ni substitution into the hausmannite structure significantly changes the mineral's reactivity toward acidity and/or As(III) oxidation, highlighting the importance of considering the effect of impurities.

2. Materials and methods

2.1. Materials

All chemical agents and reference materials for the present study were of analytical grade or better, including manganese acetate tetrahydrate (Mn(CH$_3$COO)$_2$·4H$_2$O, 99 + %, Acros Organics), nickel acetate

tetrahydrate (Ni(CH$_3$COO)$_2$·4H$_2$O, 99 + %, Acros Organics), nickel chloride hexahydrate (NiCl$_2$·6H$_2$O, 98 + %, Acros Organics), acetone (CH$_3$COOH, ≥99.5%, Thermofisher Chemicals), ethyl alcohol (C$_2$H$_5$OH, 200 proof, Pharmco-Aaper), sodium (meta)arsenite (NaAsO$_2$, ≥90%, Aldrich Chemistry), sodium arsenate dibasic heptahydrate (HNa$_2$AsO$_4$, ≥98%, Sigma Life Science), sodium chloride (NaCl, ≥99%, crystalline, certified ACS, Fisher Scientific), nitric acid (HNO$_3$, 67 to 70% (*w/w*), trace metal grade, Fisher Chemical), hydrochloric acid (HCl, 36.5 to 38% (w/w), certified ACS plus, Fisher Chemical), and sodium hydroxide (NaOH, ≥97.0%, pellet, certified ACS, Fisher Chemical). In addition, for the inductively coupled plasma-optical emission spectroscopy (ICP-OES) analysis, Mn and Ni standard solutions from J.T. Baker® (1000 μg/mL (± 0.10% *w/v*) in HNO$_3$ (< 3% w/w), reagent grade for trace metal analysis) and As standard solution from TraceCERT® (1000 mg/L (± 2 mg/L) in HNO$_3$ (2% w/w)), respectively, were used. For the As(V) analysis by ion chromatography (IC), the Dionex AS22 Eluent that contains 4.5 mM sodium carbonate and 1.4 mM sodium bicarbonate (Thermo Scientific™) was used.

2.2. Synthesis of pristine, Ni-substituted, and Ni-adsorbed hausmannite minerals

Pristine hausmannite was synthesized via a method described from the previous study with some modifications (Song et al., 2012). Briefly, a total of 2 mmol (0.49 g) Mn(CH$_3$COO)$_2$·4H$_2$O was dissolved in 5 mL of deionized (DI) water (Barnstead, 18.2 MΩ-cm water with 1–5 ppb total organic carbon) followed by the addition of 15 mL of acetone in 150 mL of the pressure glass flask. The solution was heated at 63 °C for 8 hours (h) in a silicon oil bath with stirring and then cooled to room temperature. The fresh precipitates were collected, washed with ethyl alcohol and DI water several times to remove unreacted chemical residues, and dried in the oven at 60 °C overnight. The Ni-substituted hausmannite was prepared in the same fashion as pristine hausmannite with the inclusion of 1 or 2 weight percent (wt%) from 50 mM of Ni(CH$_3$COO)$_2$·4H$_2$O along with Mn(CH$_3$COO)$_2$·4H$_2$O solution.

Samples of Ni-adsorbed hausmannite were prepared by adding 1 mM of Ni(II)Cl$_2$·6H$_2$O to 1 g/L of freshly synthesized pristine hausmannite, followed by equilibration for 24 h with pH adjustment (to pH 5) after the Ni addition. The final pH of the suspension was measured to be pH 4.7. The resulting solids were then collected, rinsed thoroughly with DI water to remove unreacted chemical residues, and dried in the oven at 60 °C overnight.

2.3. Characterization of pristine, Ni-substituted, and Ni-adsorbed hausmannite minerals

Upon the completion of synthesis, three mineral samples (pristine, 1 wt%, and 2 wt% Ni-substituted hausmannite; herein referred to as Haus, Ni1-Haus, and Ni2-Haus) were characterized for crystal structure, surface area, size, surface charge, and elemental composition. For crystal structure analysis, Ni-adsorbed hausmannite was also run to further confirm that Ni in the samples of Ni1-Haus and Ni2-Haus was structurally incorporated and not simply adsorbed on the mineral surface.

2.3.1. XRD analysis

The structure analysis of hausmannite mineral samples (pristine, and both Ni-substituted and adsorbed) was performed by PXRD measurements using a model of D8 Advance X-ray diffractometer (Bruker, USA) equipped with Ni-filtered, Cu Kα radiation and a high-speed energy-dispersive linear detector (LYNXEYE). Samples were placed on a non-diffracted Si plate holder and measured from 10 to 80° (2Θ) with a 0.01° step-size. Peak identification was performed using the DIFFRAC.EVA software with the American Mineralogy Crystal Structure Database (AMCSD). The lattice parameters of the unit cells, as well as the average particle sizes of samples were calculated with Rietveld refinement using total pattern analysis solution (TOPAS) software.

2.3.2. BET surface area analysis

The surface area of all minerals was measured in triplicate using N_2 (g) adsorption and desorption isotherm by the Quantachrome Monosorb surface area analyzer and calculated using the Brunauer-Emmett-Teller (BET) equation that was calibrated with the standard material of 1 cm³ of air (C series, Pressure lok® analytical syringe, Valco Instruments Co. Inc.). In brief, approximately 100 mg of mineral samples were used for the measurement and the samples were allowed to degas at least 30 min prior to the measurement.

2.3.3. TEM analysis

TEM analysis was performed to determine mineral size, morphology, and aggregation state with a JEOL JEM2100 TEM operated at 200 keV. TEM samples of pristine hausmannite were prepared by depositing 20–50 μL of the pre-sonicated mineral suspension onto a 400-mesh carbon-coated copper grid (Electron Microscopy Sciences, Hatfield, PA, USA) and allowed to air-dry at room temperature.

2.3.4. Zeta potential analysis

The zeta potential and point of zero charge (PZC) values of pristine hausmannite and Ni-substituted hausmannite samples were determined as a function of solution pH by using Zetasizer Nano ZSP (Malvern Instruments, Worcestershire, UK). Mineral particles were suspended in 10 mM NaCl solution at a particle loading of 0.08 g/L. The mineral suspension was then titrated with diluted HCl or NaOH to achieve a target pH from 4 to 8 and equilibrated for 24 h with pH monitoring and manual titration to maintain the target pH prior to the zeta potential measurement.

2.3.5. Elemental analysis

Elemental composition of the pristine and Ni-substituted hausmannite minerals was determined by using two different approaches. First, a microwave-assisted acid digestion technique (modified U.S. EPA method 3051A) was employed to estimate total metal concentrations of synthesized mineral samples (U.S. EPA, 2007). Specifically, a total of 10 mg of minerals were added in 10 mL of HNO_3 and were pre-digested at room temperature overnight followed by microwave-assisted digestion at 200 °C for 20 min using MARS 6 (CEM Corp.). The resulting acid digests were then analyzed by using ICP-OES for Mn and Ni quantification, which was later used to estimate the wt% of Ni in hausmannite samples.

Second, a Quanta™ 450 FEG SEM equipped with Bruker QUANTAX 400 energy dispersive X-ray spectrometer (EDX) was also employed to assess the chemical composition of the minerals. In brief, a total 10 mg of samples was dispersed into 30 mL of DI water and sonicated using a probe sonicator (Model 505 Sonic Dismembrator, Fisher Scientific™) for 10 s. About 50 μL of the dispersed mineral suspensions was dropped on the silicon wafer, dried at room temperature, and then used for the SEM analysis. Results of The SEM EDX analysis on Ni quantification can be found in Supporting Information (SI), Section 1.1 (Table S1, Fig. S1).

2.4. Batch experiments and solution analyses

Batch experiments were run with pristine or Ni-substituted hausmannite minerals at pH 5 in the absence (i.e., acidic mineral dissolution) or presence of As(III) (i.e., reductive mineral dissolution) by using established methodology (Shumlas et al., 2016). Briefly, suspensions were prepared by dispersing 30 mg of solid mineral in 149.25 mL of 10 mM NaCl solution in a 200 mL beaker. For the acidic dissolution reactions, the mineral suspensions were titrated to pH 5.0 using diluted HCl or NaOH and sonicated using a probe sonicator (Model 505 Sonic Dismembrator, Fisher Scientific™), prior to the use. For the reductive dissolution reactions, 750 μL of 50 mM As(III) ($NaAsO_2$) was added into the pH 5 sonicated mineral suspension solution, resulting in a final concentration of 250 μM of $[As(III)]_{tot}$.

Both acidic and reductive dissolution reactions were run under ambient conditions for 8 h and were completed in duplicate. A total of 11 aliquots were sampled from each replicate at selected times over the course of 8 h of reaction. Sampling involved withdrawal of a suspension aliquot, followed by syringe filtration (Millipore filter (0.22 μm)) and As (V) and total elemental analyses. The dissolved As(V) concentration was measured by IC (Dionex™, ICS-1000, Thermo Scientific) that was furnished with a Dionex IonPacAS22 analytical column (4 mm × 250 mm) and a conductivity detector. The total dissolved elemental concentration was measured by ICP-OES (iCAP 7000, Thermo Scientific), after acidification of the collected aliquots with HNO_3. For the ICP-OES analysis, the selected wavelength was used for each element, such as As (189.042 nm, axial), Mn (257.610 nm, radial), and Ni (231.604 nm, axial). At the end of each batch reaction, the reacted solids were collected by centrifugation, rinsed thoroughly, and dried under nitrogen gas (N_2) prior to solid analyses.

2.5. XAS data collection and spectral analyses

X-ray absorption spectroscopy (XAS) data were collected at the Ni, Mn, and As K-edges at two beamlines of the National Synchrotron Light Source II (NSLS II), Brookhaven National Lab (BNL), Upton, New York. The Ni K-edge spectra were collected at beamline 6-BM in fluorescence mode for unreacted Ni2-Haus after the beamline calibration with Ni foil. This is because due to the small amount of Ni in the substituted hausmannite minerals, a longer scan was needed for data collection and spectral analysis. Quick X-ray absorption spectroscopy (QXAS) data were collected at beamline 7-BM for the As-reacted samples to avoid As oxidation during XAS measurements (Nesbitt et al., 1998). The beamline was calibrated with Mn foil and Pt foil, and then the Mn and As K-edge spectra were collected at room temperature in transmission and fluorescence mode simultaneously, with a passivated implanted planar silicon (PIPS) detector for fluorescence signals. Both Mn and As K-edge XAS spectra of unreacted and/or reacted hausmannite samples were collected over the course of 5 mins, with each scan requiring 30 s.

A series of reference materials were also run under the same conditions for the XAS analysis. For Mn speciation, birnessite (MnO_2) (McKenzie, 1971) and manganite (MnOOH) (Hu et al., 2008) were used after they were synthesized in the laboratory via a method described from the cited papers. For As speciation, $NaAsO_2$, HNa_2AsO_4, and As (V)-reacted hausmannite were used as reference materials. As(V)-reacted mineral samples were prepared by adding 750 μL of 50 mM As(V) (HNa_2AsO_4) into the pH 5-adjusted hausmannite particle suspension. For Ni speciation, bunsenite (NiO, U.S. research nanomaterial[INC]), nickel chloride hexahydrate (99.999% for analysis, Acros Organics™), and theoparastite ($Ni(OH)_2$) were used. In the case of theoparastite, Ni $(OH)_2$, it was synthesized in the laboratory by titrating 1 M $NiCl_2$ solution into alkaline DI water (pH 9). After centrifugation and drying, PXRD was run on the collected precipitates and confirmed the formation of theoparastite, $Ni(OH)_2$.

Data processing was conducted with Artemis and Athena (Ravel and Newville, 2005). The X-ray absorption near-edge structure (XANES) spectra for all target elements (Ni, As, and Mn) were averaged, normalized, and, background-corrected using the Athena interface (Ravel and Newville, 2005). The extended X-ray absorption fine structure (EXAFS) $\chi(k)$ spectra were calculated with k^3 weighting in the approximate range from about 3.0–9.0 Å^{-1} for Ni K-edge and As K-edge and 3.0–12.0 Å^{-1} for Mn K-edge. Crystal information files were obtained from the American Mineralogy Crystal Structure Database (AMCDS) and run with ATOMS and FEFF to calculate theoretical scattering pathways for fitting.

2.6. Flow-cell ATR-FTIR spectra analysis

The ATR-FTIR measurements were carried out with a Smart Orbit ATR diamond accessory housed in a Nicolet 6700 spectrometer (Thermo Scientific™) equipped with a liquid N_2-cooled MCTA detector following established procedures in the literature (Bhandari et al., 2011, 2010; Cerkez et al., 2015). Experiments were conducted by

depositing ~75 to 100 μL of a mineral suspension (~0.8 mg of mineral in the suspension) on the ATR element, following by drying under $N_2(g)$. After drying, a house-made Teflon flow cell was placed around the film. After equilibration (indicated by constant spectra), three different solution types were introduced to the mineral films for 2 h at a flow rate of 1 mL/min, including (i) 10 mM NaCl (pH 5 and no As; acid dissolution), (ii) 10 mM NaCl with 250 μM As(III) (pH 5; reductive dissolution), and (iii) 10 mM NaCl with 500 μM As(V) (pH 5; a reference for As (V) speciation). Spectra were collected from 650 to 4000 cm^{-1} with the resolution of 4 cm^{-1} (200 co-added scans). All spectra were processed by subtracting the background spectra before introduction of As(III) or As(V). It is noted that due to low As(V) adsorption on the mineral surface, the As(V) concentration was doubled in (iii) to improve signal to noise ratio for better presentation.

3. Result and discussion

3.1. Effects of Ni substitution on hausmannite structure and characteristics

The effects of Ni substitution on the hausmannite structure and characteristics were systematically examined by comparing Ni-substituted hausmannite to pristine hausmannite. Of interest were changes in the crystalline structure, particle size, and surface area induced by Ni substitution into the hausmannite structure.

First, PXRD patterns of Ni-substituted hausmannite minerals matched that of the pristine and the reference material (Mn_3O_4), indicating that no other mineral phases were present in the samples (Fig. 1). However, Ni substitution into the hausmannite structure resulted in peak shifting and sharpening in PXRD reflections, which are more significant at 2 wt% than 1 wt% substitution (Figs. 1 and S2). The positions of main peak of Ni-substituted hausmannite shift slightly toward higher 2θ than those of pristine.

To further confirm that Ni was structurally incorporated and not simply adsorbed on the mineral surface, PXRD patterns were collected for Ni-adsorbed hausmannite (i.e., Ni(II)$_{aq}$ introduced after the hausmannite synthesis). These patterns were essentially identical to that of the pristine phase, and lacked the slight changes observed for the Ni-substituted phase (Fig. S2). Peak shifting and sharpening observed in PXRD reflections of Ni-substituted hausmannite can be attributed to differences in lattice size, changes in crystal strain, as well as increases in particle size induced by Ni substitution. Specifically, the derived unit cell lattice parameters of Ni-Haus samples deviated from those of pristine, most noticeably in the *c*-axis value decreasing with increased substitution percentage (Table S2). In addition, the *c/a* ratio calculated from the unit

cell lattice parameters decreased as a result of Ni substitution.

These changes in lattice parameters are presumably due to the combined results of replacing a larger, Jahn-Teller distortion inactive Ni (II) with a smaller Jahn-Teller distortion active Mn(III) ions in the structure (Shannon, 1976). This also suggests that this substitution induced a compressed octahedral geometry along the c-axis but stretched a tetrahedron and thus, accommodating associated changes in the Jahn-Teller distortion and symmetry by Ni substitution. Secondly, Ni substitution in the hausmannite structure also had an impact on particle size and surface area of the mineral. The results of Rietveld refinement analysis showed an increase in the average particle sizes of hausmannite samples with increasing levels of Ni substitution (Table S2). The results of TEM analyses on pristine hausmannite also support this particle size estimation, recording an average particle size of 21.1 (± 4.8) × 16.7 (± 3.7) nm (a total of 516 nanoparticles across two different TEM grids were used for this size analysis) (Fig. S3). The increase in particle size by Ni substitution resulted in lowering the mineral's specific surface area: Pristine hausmannite recorded the highest BET surface area, 136 m^2/g, whereas those of Ni1-Haus and Ni2-Haus were measured as 102 and 97.6 m^2/g, respectively. A decrease in surface area by metal substitution is noted with other Mn oxide systems (Wu et al., 2019).

3.2. Effects of structural impurities on hausmannite dissolution

3.2.1. Acidic dissolution of pristine and Ni-substituted hausmannite at pH 5

The effect of Ni substitution on the reactivity and stability of hausmannite was assessed by measuring the extent of the acidic dissolution of pristine and substituted minerals at pH 5. All minerals readily underwent dissolution at this pH, as evidenced by the release of aqueous Mn(II) (Table S3), which agrees well with previous investigations on hausmannite dissolution (Luo et al., 2018). Of note was a relative increase in [Mn(II)]$_{aq}$ observed in the experiments with Ni-substituted hausmannite compared to pristine hausmannite despite a lower BET surface area of the Ni-substituted hausmannite. Release of Mn from the Ni-substituted hausmannite was accompanied by concomitant release of Ni, with higher Ni concentrations from Ni2-Haus than Ni1-Haus. Further, the fraction of Ni of the total metal released, [Me], was estimated to be 0.01 and 0.03 for Ni1-Haus and Ni2-Haus, respectively, consistent with the fraction of Ni substitution in hausmannite structure (SI, Section 3.2.1 and Table S3). This further indicates that the majority of Ni remained in hausmannite structure after the 8-h acidic dissolution, which agreed with the results of the Ni mass balance calculation (Table S4). Once released, Ni tends to remain in solution instead of re-adsorbing onto the hausmannite surface. The PZC values of Haus and
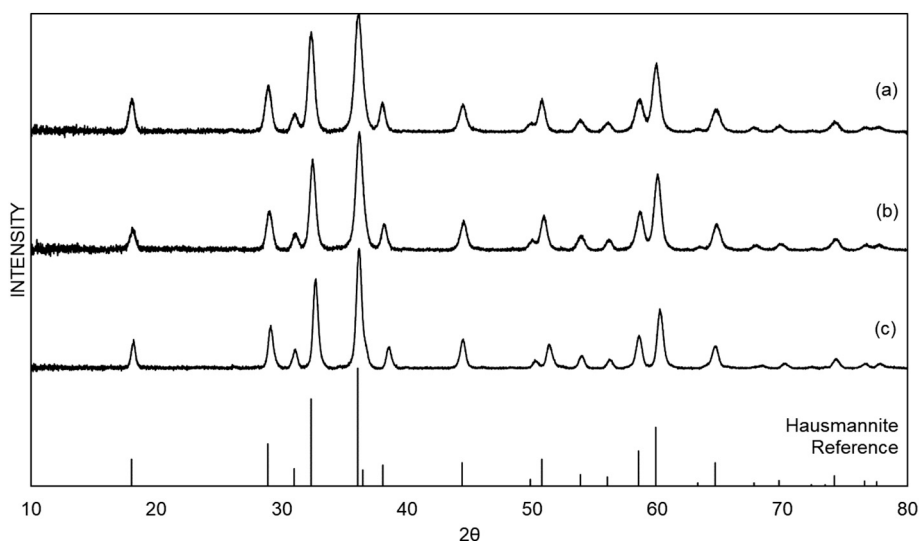

Fig. 1. Full PXRD spectra of pristine hausmannite and Ni substituted-hausmannite minerals (2θ from 10 to 80°); (a) pristine hausmannite, (b) 1 wt% Ni substituted-hausmannite, (c) 2 wt% Ni substituted-hausmannite. The reference material, Mn_3O_4, hausmannite (AMCSD #0002024) was used for mineral identification.

Ni2-Haus minerals are estimated of pH 4.1 to 4.6 (Fig. S4), and hence, at pH 5 Ni(II) adsorption would not be favored on neutral or slightly negative mineral surfaces. Furthermore, mineral surfaces continue to undergo acidic dissolution at pH 5, which may alter their adsorptive behaviors. Thus, enhanced release of structural Mn and Ni observed in the substituted minerals suggests an increase in hausmannite reactivity and a decrease in stability resulting from by Ni substitution, making the mineral more susceptible to acidic dissolution.

3.2.2. Reductive dissolution of pristine and Ni-substituted hausmannite by arsenite at pH 5

The extent of reductive dissolution of pristine and Ni-substituted hausmannite was measured using arsenite (As(III)) as the reductant to ascertain the effect of Ni substitution on the mineral's reactivity and stability. Stoichiometrically, 2 mol of Mn(III) in hausmannite oxidize 1 mol of As(III), producing 2 mol of Mn(II) and 1 mol of As(V) (Eq. (1)).

$$2\,Mn(III) + As(III) \rightleftharpoons 2\,Mn(II) + As(V) \qquad (1)$$
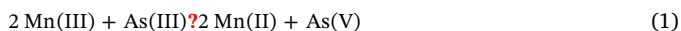
For Ni-substituted hausmannite, it is therefore of interest to determine (1) whether release of structurally-incorporated Ni occurs concomitantly with Mn(II) release and (2) if the stoichiometric relation between Mn(II) and As(V) is affected by Ni substitution. As shown in the previous section, hausmannite undergoes acidic dissolution at pH 5, and acidic dissolution is assumed to occur to some extent during reductive dissolution as well since the experiments were conducted at the same pH. Therefore to quantify the extent of the reductive dissolution by As(III), the aqueous concentrations of Mn and Ni were estimated by subtracting the initial concentration of these elements measured prior to the addition of As(III).

Introduction of As(III) into suspensions of pristine and Ni-substituted hausmannite caused mineral reductive dissolution, as shown in Fig. 2(a). The largest release of $[Mn(II)]_{aq}$ was observed in Ni2-Haus, followed by Ni1-Haus, and finally Haus, with concentrations of 441 (± 27), 431 (± 49), and 362 (± 11) μM, respectively (Fig. 2(a), square).

Compared to the acidic dissolution reaction, more release of aqueous Mn was observed in these reduction experiments. During reductive dissolution structural Ni was released as well at levels of 13.4 (± 0.5) and 4.25 (± 0.77) μM from Ni2-Haus and Ni1-Haus, respectively (the inset figure in Fig. 2(a)). More aqueous Ni(II) was also released from the Ni-substituted minerals during reductive dissolution than during acidic dissolution. However, the fraction of aqueous Ni to total metal released was similar as observed during acidic dissolution, at a value of 0.01 and 0.03 for Ni1-Haus and Ni2-Haus, respectively (SI, Section 3.2.3). Mass balance calculations show that 81.1–82.7% of added Ni remained in hausmannite structure after the 8-h reductive dissolution reaction with As(III) (Table S5). This represents a noticeably stronger decrease in total Ni percentage remaining in hausmannite than in the acidic dissolution experiments described in the previous section. Over the course of the reductive dissolution reactions, oxidation of As(III) to As(V) occurred, and the concentrations of aqueous As(V) (i.e., $[As(V)]_{aq}$) increased over the experimental duration in all experiments (closed triangle, Fig. 2(b)).

To effectively examine the effect of Ni substitution on As(III) oxidation, the measured $[As(V)]_{aq}$ at a given sampling time was normalized to the measured BET surface area of each mineral (Fig. 2(b), an inset figure). While Ni2-Haus recorded the lowest BET surface area, Ni2-Haus showed the highest efficiency for As(III) oxidation, followed by Ni1-Haus and then pristine Haus, indicating that the presence of Ni in the structure enhanced the oxidative ability of hausmannite. The increase in oxidizing ability of hausmannite resulting from Ni substitution facilitates the extent of mineral dissolution in the presence of As(III), evidenced by a large quantity of Mn(II) and Ni(II) released from the substituted than the pristine mineral.

Once oxidized, more than 75% of total As added remained in solution after 8 h, indicating that only a relatively small proportion of total As adsorbed onto the mineral surfaces (open triangle, Fig. 2(b)). This lack of interaction between As(V) and the mineral surfaces can be explained by electrostatic effects. The PZC values of pristine Haus and Ni2-Haus were

estimated at pH 4.1 and 4.6 (Fig. S4), consistent with previous study (Weaver and Hochella, 2003). Therefore at pH 5, both arsenate ($pK_{a1} = 2$, $H_2AsO_4^-$, $pK_{a2} = 6.8$, $HAsO_4^{2-}$) and the hausmannite surface are negatively charged, and hence, interactions are not favored, whereas the neutral arsenite moiety ($pKa_1 = 9$, H_3AsO_3) would still be expected to interact with the negatively charged mineral (Smedley and Kinniburgh, 2002). This finding is consistent with prior work where birnessite surfaces were not favorable for As adsorption (Shumlas et al., 2016).

Under the current conditions, a Mn(II):As(V) ratio of 1.9:1 was calculated for the pristine mineral, and of 2.0:1 and 2.2:1 for the Ni2-Haus and Ni1-Haus minerals. These are close to the 2:1 ratio predicted from the theoretical stoichiometry of reductive dissolution (Eq. (1)). As noted above, more than 75% of total As added remained in solution after 8 h, and hence, less than 25% of total As was present as adsorbed As(V) on the mineral surface. This can be also be seen in Fig. 2(b), where total measured aqueous As concentrations (open triangle) were all close to the 250 μM level of total As(III) added. However, when accounting for the relatively small As(V) fraction retained on the surface in the calculation of redox stoichiometry, the estimated Mn(II):As(V) ratios are 1.6:1, 2.0:1, and 2.0:1 for Haus, Ni1-Haus, and Ni2-Haus, respectively. Thus while the Ni-substituted samples produce the predicted stoichiometric ratios of Mn(II):As(V), the ratio of the pristine sample is lower than expected.

In order to quantify the effect of Ni substitution in hausmannite on the rate of mineral reductive dissolution, we estimated the rate of Mn release for both pristine and Ni-substituted phases by using total dissolved Mn concentration (closed square, Fig. 2(a)) after the surface area normalization over the reaction times. Since all the samples display a similar pattern of Mn release, initially fast but slowing after 1 h, we estimated the two rates of Mn release by each mineral, initial and subsequent reaction rates (less than 1 h vs 1–8 h) (Table S6). When comparing the initial rates in Mn release of the pristine and Ni-substituted phases, the differences are estimated to range from 87.0% to 100%, suggesting that all hausmannite samples display similar rates in the initial stage of the reductive dissolution. However, the differences in the rates by pristine and Ni-substituted hausmannite are much greater, varying from 55.8% to 100%, when comparing the following rates (i.e., secondary reaction rates, 1–8 h). In other words, a substantial decrease in Mn release was noted from pristine hausmannite, compared to that of Ni-substituted hausmannite as the reaction proceeded. Thus, this finding suggests that Ni substitution in the hausmannite structure promotes accelerated mineral dissolution in the presence of As(III), resulting in more Mn release than the pristine phase.

3.3. XAS analysis of pristine and Ni-substituted hausmannite before and after dissolution reactions

The results of PXRD analysis suggest that Ni incorporation occurs at Mn(III) octahedral sites in hausmannite structure. However, there has been disagreement in literature in regard to site occupancy of Ni in hausmannite, with some studies suggesting Ni occupancy at the tetrahedral sites (Chasserio et al., 2007; Dong et al., 2013; Maruthapandian et al., 2016), but others at the octahedral sites (Chasserio et al., 2007; McKenzie, 1972). To examine the Ni coordination chemistry, we employed XANES and EXAFS analyses at the Ni *K*-edge of mineral solids before dissolution reactions. Furthermore, because of the pronounced effects of Ni substitution on reductive dissolution (see previous section), we focused on samples retrieved from the reductive dissolution experiments for As *K*-edge XAS analyses. Due to the trace levels of Ni substitution in hausmannite structure and limited adsorption of As on the hausmannite surfaces, the results of Mn *K*-edge analysis before and after the reductive dissolution reactions provided little information, and hence, were provided in the SI, Section 3.3.1 (Figs. S5, S6 and Table S7).

3.3.1. Ni K-edge XANES and EXAFS before and after reductive dissolution reaction

The XANES spectra obtained at the Ni *K*-edge (Fig. 3(a)) show that unreacted Ni2-Haus aligned with the spectra of bunsenite (NiO) and Ni
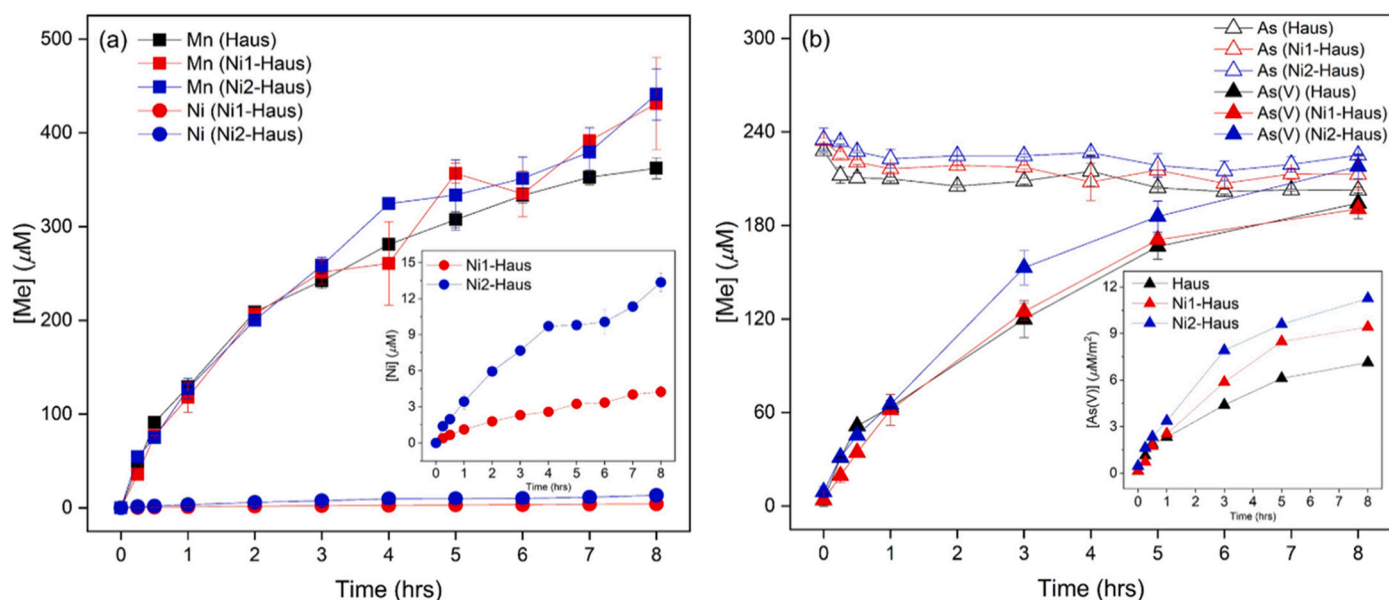
Fig. 2. (a) Total dissolved concentration of metals from Haus (black), Ni1-Haus (red) and Ni2-Haus (blue) (i.e., $[Mn(II)]_{aq}$ (square) and $[Ni(II)]_{aq}$ (circle)), with the enlarged figure of $[Ni(II)]_{aq}$ as a function of time and (b) total dissolved As (open triangle) and $[As(V)]$ (closed triangle) with the inset figure of the surface area normalized As(V) production as a function of time.

(II)-hydroxide, confirming that substituted Ni is divalent, as expected. In regard to Ni incorporation in hausmannite structure, the EXAFS region of Ni substituted hausmannite (Fig. 3(b)) shows significant deviation from bunsenite (NiO) and Ni(II)-hydroxide, which is also reflected in the fit results (Table 1). This finding agrees with our PXRD results suggesting Ni being structurally incorporated in hausmannite and not forming secondary phases such as Ni (hyrd)oxides. For the coordination chemistry of Ni, two scattering pathways from Ni *K*-edge, Ni—O and Ni-Me, were fitted for Ni-substituted hausmannite. For the Ni—O pathway, the best fit was found when using a split oxygen shell with the coordination numbers (CN) fixed at 6 (with 4 equatorial oxygen and 2 axial oxygen). The best fitted equatorial and axial oxygen radial distances of substituted Ni were found to be 2.08 Å and 2.24 Å, respectively, indicating Ni occupancy at the Jahn-Teller distorted Mn (III) octahedral sites, as opposed to Mn(II) tetrahedral sites (Table 1 in the present study, Hens et al., 2018). In addition, the Ni *K*-edge fitting from Ni in tetrahedral sites was failed during the fitting procedure (data not shown). Furthermore, the ratio of the fitted axial to equatorial oxygen radial distances of substituted Ni is 1.08, which is smaller than the theoretical value for Mn(III) in pristine hausmannite, which is 1.18. The closer the ratio is to one, the more symmetrical the octahedral geometry; therefore, octahedral Ni(II) is more symmetrical than octahedral Mn(III). The increased symmetry of Ni-hausmannite can be attributed to a relaxing of the Jahn-Teller distortion, as is expected for Ni (II) octahedra relative to Mn(III) octahedra. This also agrees well with our previous PXRD results where Ni substitution induced a compressed octahedral geometry along the *c*-axis, resulting in changes in the Jahn-Teller distortion and symmetry. While the 2nd shell scattering is much dominated by Mn due to insignificant contributions from the trace level of Ni substitution, the distance of Ni-Me (3.03 Å) is well matched with the crystallographic value of octahedral site (average 3.04 Å) rather than the one of tetrahedral site (3.44 Å) (Table 1), suggesting the presence of Ni in the octahedral site. Similar to our results, previous studies also indicate that Ni is preferentially incorporated into the octahedral sites in spinel structured minerals or Mn-(hydr)oxides (Burdett et al., 1982; Manceau et al., 1987; Manceau and Calas, 1986; Urusov, 1983).

We also note that after reductive dissolution by As(III), XANES analysis of the Ni *K*-edge spectra of Ni-substituted minerals showed little to no change in features or locations of the corresponding absorption edges, indicating that the oxidation states of structural Ni

remained the same before and after the dissolution reaction (Fig. S7). This similarity in XANES features also agrees with the batch reaction results, where the majority of Ni remained situated in the hausmannite structure after 8-h dissolution reactions.

3.3.2. As K-edge XAS after reductive dissolution reaction

The positions of the As XANES spectra of all As(III)-reacted minerals match that of the As(V)-reacted hausmannite reference, located at 11873 eV (Fig. 4(a)). This demonstrates that the only As species in the samples is As(V). This agrees with the solution analyses described above, where we observed that the majority of added As(III) was converted to As(V). These results are also in agreement with previous XAS studies which noted that As(III) adsorption/oxidation by Mn-oxides resulted in only As(V) on the mineral surfaces (Lafferty et al., 2010; Manning et al., 2002; Shumlas et al., 2016; Tournassat et al., 2002; Wu et al., 2018). Additionally, the exclusive presence of As(V) on the surface supports the Mn(II):As(V) ratios discussed above; that is, the quantity of As(V) adsorbed on the mineral surfaces accounts for the difference between total added As and total aqueous As measured after 8 h in the batch studies.

To examine the coordination environment of As(V) on the mineral surface, the As *K*-edge EXAFS spectra were analyzed and the fitting parameters were determined (Fig. 4(b), (c), and Table 2). Shell-by-shell fits were performed with two scattering pathways from As *K*-edge spectra, As—O and As—Mn, for As(III)-reacted Haus, Ni1-Haus, and Ni2-Haus, as well as As(V)-reacted Haus. The shell-by-shell fitting results of As(III/V)-reacted Haus were provided in Fig. S8. The fitting results of As (III)-reacted Ni1-Haus and Ni2-Haus were similar to those of As(III/V)-reacted Haus samples, and hence, were not provided. The 1st shell was attributed to backscattering from four O atoms at a distance of 1.68 Å, consistent with previous work (Lafferty et al., 2010; Manning et al., 2002; Wu et al., 2018). A 2nd shell, attributed to As(V)-Mn, was fitted at a radial distance of ~3.35 Å for the Haus, Ni1-Haus, and Ni2-Haus samples. This distance is consistent with As(V) adsorbed as a BB surface complex, in good agreement with the results of the Mn *K*-edge EXAFS analysis from other studies (Lafferty et al., 2010; Manning et al., 2002). The similarity in results obtained for the pristine and Ni-containing samples demonstrates that there is no significant difference in As(V) coordination resulting from Ni substitution.

The fit results of the sample where sorbate As was introduced directly as As(V) yielded a As(V)-Mn distance of 3.28 Å (Table 2). This
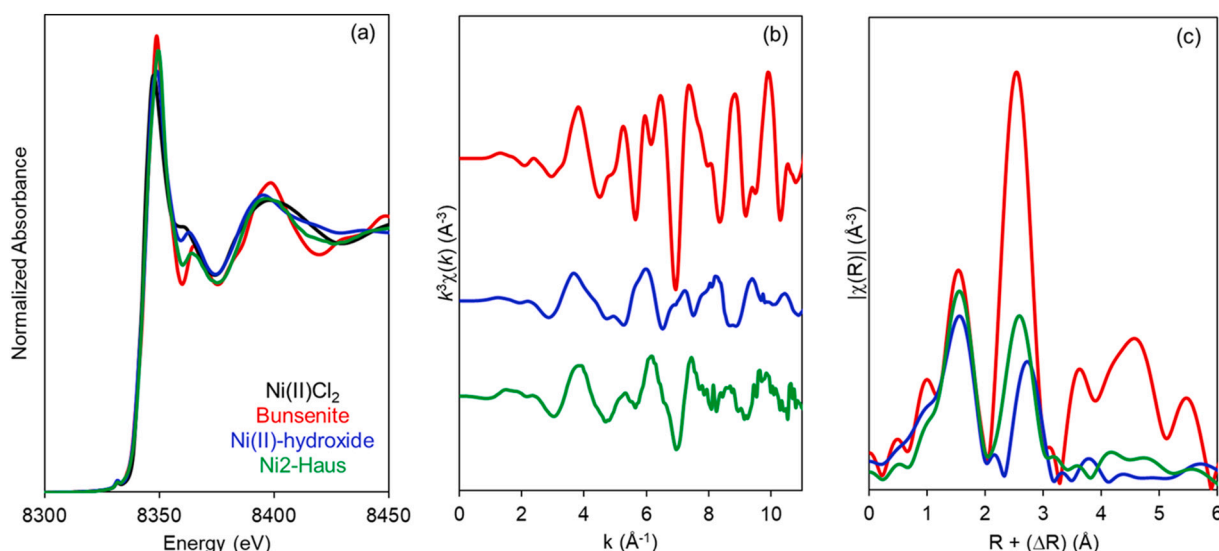
Fig. 3. Ni *K*-edge X-ray absorption spectra. (a) XANES of NiCl$_2$ (black), bunsenite (NiO, red), Ni(OH)$_2$ (blue), and Ni2-Haus (green) and EXAFS of bunsenite, Ni(II) hydroxide, and Ni2-Haus in (b) *k*^{3}-weight χ(*k*) function, and (c) the radial distance from center atom of Ni.

distance is slightly shorter than the As(V)-Mn distance observed in As (III)-reacted hausmannite forming BB configuration on surface. This slight reduction in distance may be the result of the variation in surface complexation of As(V) species discussed further in the next section.

3.4. In-situ observation of dissolution reactions by ATR-FTIR

As a complementary technique to XAS analysis, in-situ time resolved ATR-FTIR was performed to study surface complexation and structural changes occurring on or near the mineral surface during dissolution reactions. When simulating acidic solution conditions (i.e., pH 5) for 2 h the only vibrational mode observed was a minor peak located at 925 cm^{-1}, which may be due to a possible formation of Mn-hydroxide (Fig. S9(A), a minor peak between two dotted lines) (Elzinga, 2011). However, no vibrational bands were observed between 1080 and 1150 cm^{-1}, which is the spectral region where intense manganite bands occur (Elzinga, 2011).

To analyze the reductive dissolution of hausmannite by As, arsenite and arsenate were both to the pristine and Ni-substituted hausmannite samples. Aqueous batch reactions from this study, and previous ATR work on birnessite, demonstrate that the oxidation of As(III) to As(V) is facile and rapid, and therefore vibrational modes associated with the arsenite moiety are not observed on Mn oxides (Parikh et al., 2008). In contrast, three fundamental vibrations of the tetrahedral As(V) species when doubly protonated were expected, including the symmetric (ν$_s$) As−O stretch located at ~875 cm^{-1}, the corresponding antisymmetric (ν$_{as}$) stretch located at ~908 cm^{-1}, and a broad band located between

~759–766 cm^{-1} representing the ν$_s$ + ν$_{as}$ of As-OH. Here when As(V) (H$_2$AsO$_4$$^-$) was exposed to the hausmannite surface a broad absorption was observed between 900 and 700 cm^{-1} (Fig. 5A). The expected vibrations are located within this envelope and the broadness and blending of the peaks is attributed to decreases in symmetry caused by complexation to the varied Mn centers (Mn(II/III)) at the hausmannite surface, as previously hypothesized (Silva et al., 2013). While the EXAFS analysis showed As(V) BB configuration to be dominant on the hausmannite surfaces, in-situ observation by ATR-FTIR may suggest the formation of more than one type of surface complex. The swath of possible adsorption complexes thus may include various bidentate, monodentate, binuclear, and mononuclear moieties, as well as changes made by protonation of the adsorbed species.

The exposure of As(III) to pristine or Ni-substituted Haus resulted in the growth of two vibrational modes at 895 and 750 cm^{-1} within the first 10 min of exposure (Fig. 5B and C). By analyzing the spectral difference between subsequent time points, the intensity of these bands was shown to be correlated; the modes increase in intensity at the same rate over the initial 40 min of surface exposure and reach maxima at the same time point. The lack of continual growth of these two vibrations indicates that the surface becomes saturated, where no further As was retained on the surface, consistent with post-batch reaction analysis indicating small As loadings on the mineral surfaces. The locations of the two peaks were assigned to a BB inner sphere complex of arsenate bound to octahedral centers on the hausmannite surface, consistent with aforementioned EXAFS results, and prior works (Lafferty et al., 2010; Manning et al., 2002; Silva et al., 2013). No shift in the position

Table 1

Ni *K*-edge EXAFS spectra fitting parameters and results of Ni2-Haus and comparison to the relevant crystallographic values of Mn−O and Mn−Mn from hausmannite.

Ni2-Haus*				Crystallographic values (hausmannite)[a]					
				Octahedral			Tetrahedral		
Shell	CN[b]	R (Å)	σ^2 (A^2)	Shell	CN	R (Å)	Shell	CN	R (Å)
O	4	2.08 (15)	0.006 (2)	O	4	1.93	O	4	2.04
O	2	2.24 (4)	0.013 (9)	O	2	2.28			
Me (6)	6	3.03 (14)	0.012 (1)	Mn (6)	2	2.89	Mn (6)	8	3.44
				Mn (6)	4	3.12			

[a] The crystallographic values, interatomic distances and CN were obtained from crystal information file of hausmannite in the AMCDS.

[b] CN was fixed during the fitting analysis. R is radial distance. The σ^2 (A^2) is the Debye-Waller factor. All parameters are reported with estimated uncertainties for the fitting exercises (provided in the parentheses in the table), except fixed parameters.

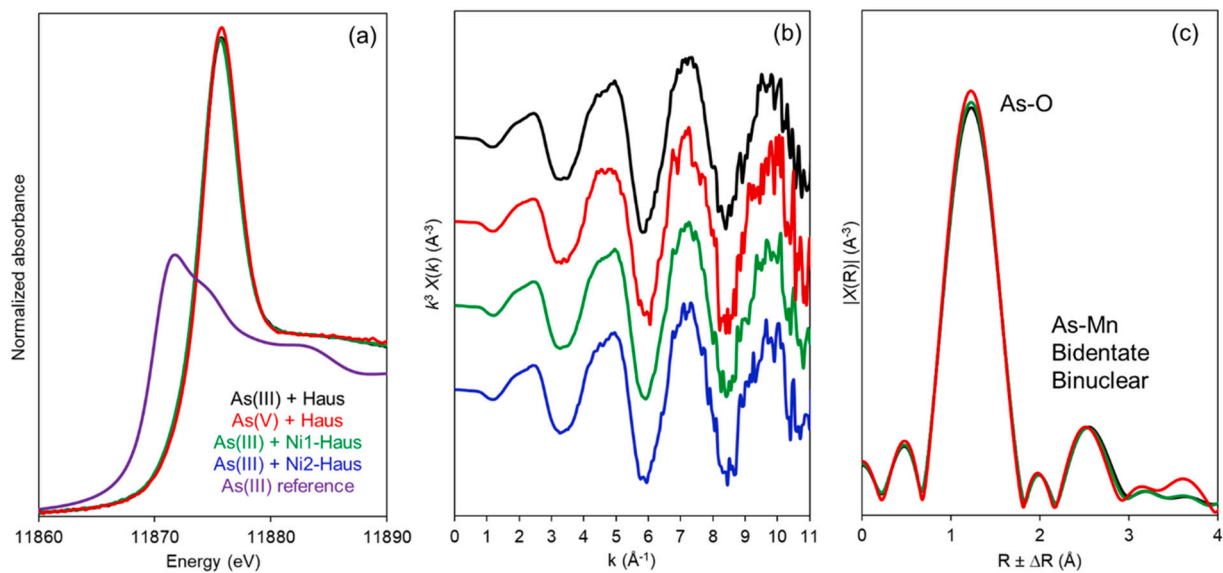* R-factor was 0.006 and ΔE° was −2.50 (± 1.12) from the fitting result.

Fig. 4. As *K*-edge X-ray absorption spectra. (a) XANES spectra of As(III)-reacted pristine and Ni-substituted hausmannite samples and of As(V)-reacted hausmannite (As(V) reference compound, red), and NaAsO$_2$ (As(III) reference compound, purple), and (b) k^3-weighted and (c) radial distance (R) of EXAFS spectra of As(III)-reacted pristine and Ni-substituted hausmannite and of As(V)-reacted hausmannite (reference compound, red).

Table 2
As *K*-edge EXAFS spectra fitting parameters and results for As(III)-reacted Haus and Ni-substituted Haus.

Agent	Sample	As-O			As-Mn		
		CN[a]	R (Å)	σ^2 (A^2)[b]	CN	R (Å)	σ^2 (A^2)
As(III)	Haus	4	1.68 (2)	0.002 (1)	2	3.34 (6)	0.007 (16)
	Ni1-Haus	4	1.68 (2)	0.0004	2	3.34 (5)	0.009 (18)
	Ni2-Haus	4	1.68 (1)	0.0004	2	3.35 (11)	0.01 (21)
As(V)	Haus	4	1.68 (2)	0.0004	2	3.28 (66)	0.009 (18)

[a] CN was fixed during the fitting analysis. R (radial distance) and its uncertainty is marked with ΔR. The σ^2 (A^2) is the Debye-Waller factor. All parameters are reported with estimated uncertainties for the fitting exercises (provided in the parentheses in the table), except fixed parameters.

[b] The fitting for the 1st shell was conducted with $\sigma^2 = 0.0004$ to avoid the violation in fitting exercise.

of the peaks as a function of surface was evident, indicating the As(V) bound to the surface is most likely confined to Mn octahedra, as binding to Ni octahedra would be expected to shift the vibration due to changes in As-O-Me bond strength. Because of similar observations between As(III)-reacted Ni1-Haus and Ni2-Haus, the Ni1-Haus ATR-FTIR result is provided in the SI (Fig. S9B).

After 40 min, the pristine Haus surface shows little variation with continued As(III) exposure. In contrast, the Ni-substituted Haus minerals display growth of vibrational modes located below 750 cm^{-1}. Spectral difference analysis isolates this growth to an absorbance located at ~679 cm^{-1}. A broad search of previous work shows no reasonable attribution to an adsorbed arsenic moiety and thus the change is assigned to perturbations occurring at the mineral surface. In general, the vibrational modes of the MnO$_6$ octahedra are found between 400 and 700 cm^{-1} with additional bands in the low wavelength regions (Julien et al., 2004). However, 679 cm^{-1} is not assigned to any of the vibration modes reported for known Mn oxide minerals. Since this vibrational
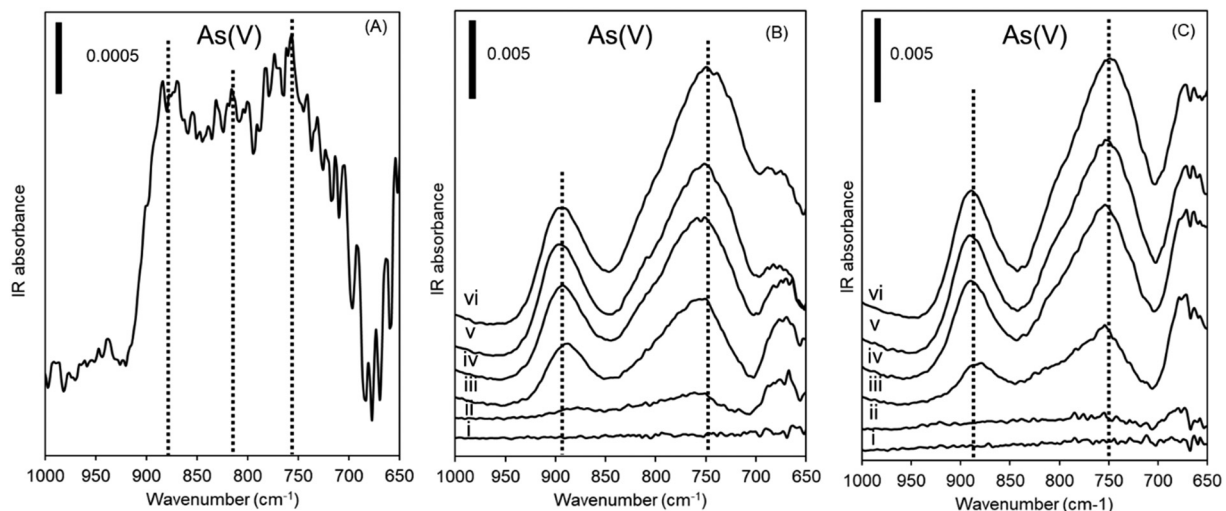

Fig. 5. Flow cell in-situ ATR-FTIR results from (A) As(V)-reacted hausmannite (measured in a static condition), (B) As(III)-reacted pristine Haus, and (C) As(III)-reacted Ni2-Haus at baseline (i) time 0 (ii) 10 (iii), 30 (iv), 60 (v), and 120 (vi) minutes.

mode was absent during acidic dissolution in both pristine and Ni-substituted hausmannite (where Mn(III) reduction does not occur) and the intensity of the vibrational mode in Ni-substituted hausmannite was increased relative to the pristine surface, we suspect that this may be related to the changes in the vibration modes of Mn—O associated with the Mn(III) reduction, more intensified in the presence of structural Ni. Similar to the observed changes in lattice parameters, increased symmetry in the octahedral geometry and lowered Jahn-Teller effects on Ni-substituted hausmannite detected by the bulk analysis, this vibrational mode may be attributed to the changes in surface structures through the formation of lower symmetry of edge sharing octahedron and/or under-coordinated octahedron induced by Ni substitution. These transient structural configurations are known to be highly reactive sites for the dissolution reactions and can only be detected by in-situ time-resolved analysis. This finding is also in agreement with the results of the estimated rates of Mn(II) release and the stoichiometric ratios of Mn(II):As (V), where Ni-substituted samples produced higher Mn release rates than the pristine phase and meets the stoichiometric ratio, indicating the minerals continue to sustain the reactions. Thus, the higher As(III) oxidizing ability and enhanced reactivity to acidity observed in Ni-substituted hausmannite may be attributed to the generation of those unsatisfying reactive sites as the oxidation reaction proceeds.

4. Conclusion and environmental implications

Natural Mn oxides commonly have structural impurities; however, the impacts of metal substituents on the geochemical behaviors of Mn(II/III) oxides have never been experimentally assessed. The present study investigated hausmannite ($Mn^{II}Mn^{III}_2O_4$), the most widely distributed spinel structured Mn oxide in the environment, and demonstrates for the first time that the incorporation of trace metal Ni(II) strongly affect the stability and redox reactivity of this mineral. This suggests that the presence and availability of trace metal structural impurities play a key role in regulating the solubility of Mn(II/III)-oxides and cycling of transition metals and metalloids in aqueous geochemical environments.

Similar to Ni-substituted hausmannite, Ni-substituted magnetite (Fe_3O_4), a common spinel structured iron oxide, also revealed that structural incorporation of Ni in magnetite leads a partial elimination of the Jahn-Teller distortion in the mineral, resulting in changes in the magnetic behavior deviated from that of pristine magnetite as increasing Ni contents (Deepak et al., 2015). While the present investigation focuses on Ni, as a metal substituent, future investigations on structural incorporations of redox-labile elements, such as cobalt (Co) and iron (Fe), in hausmannite, and their effects on the mineral's reactivity and stability will be of interest. Based on the effects of Ni substitution on the oxidizing ability of hausmannite observed here, structural incorporation of redox-labile elements in hausmannite may also expect to alter the rates and/or products of reduction-oxidation reactions of inorganic and organic compounds in geologically-relevant settings. Thus, this study showcases that it is important to consider the effects of structural impurities to better predict the behavior and reactivity of natural Mn(II/III) oxides and related phases in complex surficial environments.

Declaration of competing interest

The authors declare that they have no known competing financial interests or personal relationships that could have appeared to influence the work reported in this paper.

Acknowledgement

Appendix A. Supplementary data

Supplementary data to this article can be found online at https://doi.org/10.1016/j.chemgeo.2020.119862.

References

Bhandari, N., Hausner, D.B., Kubicki, J.D., Strongin, D.R., 2010. Photodissolution of ferrihydrite in the presence of oxalic acid: an in situ ATR-FTIR/DFT study. Langmuir 26, 16246–16253.

Bhandari, N., Reeder, R.J., Strongin, D.R., 2011. Photoinduced oxidation of arsenite to arsenate on ferrihydrite. Environ. Sci. Technol. 45, 2783–2789.

Burdett, J.K., Price, S.L., Price, G.D., 1982. Role of the crystal-field theory in determining the structures of spinels. J. Am. Chem. Soc. 104, 92–95.

Burns, R.G., 1993. Mineralogical Applications of Crystal Field Theory, 2nd ed. Cambridge University Press, Cambridge.

Cerkez, E.B., Bhandari, N., Reeder, R.J., Strongin, D.R., 2015. Coupled redox transformation of chromate and arsenite on ferrihydrite. Environ. Sci. Technol. 49, 2858–2866.

Chao, T.T., 1976. The significance of secondary iron and manganese oxides in geochemical exploration. Econ. Geol. 71, 1560–1569.

Chapnick, S.D., Moore, W.S., Nealson, K.H., 1982. Microbially mediated manganese oxidation in a freshwater lake. Limnol. Oceanogr. 27, 1004–1014.

Chasserio, N., Durand, B., Guillemet, S., Rousset, A., 2007. Mixed manganese spinel oxides: optical properties in the infrared range. J. Mater. Sci. 42, 794–800.

Chukhrov, F.V., 2006. Manganese minerals in clays: a review. Clay Clay Miner. 28, 346–354.

Deepak, F.L., Bañobre-López, M., Carbó-Argibay, E., Cerqueira, M.F., Piñeiro-Redondo, Y., Rivas, J., Thompson, C.M., Kamali, S., Rodríguez-Abreu, C., Kovnir, K., Kolenko, Y.V., 2015. A systematic study of the structural and magnetic properties of Mn-, Co-, and Ni-doped colloidal magnetite nanoparticles. J. Phys. Chem. C 119, 11947–11957.

Dong, R., Ye, Q., Kuang, L., Lu, X., Zhang, Y., Zhang, X., Tan, G., Wen, Y., Wang, F., 2013. Enhanced supercapacitor performance of Mn_3O_4 nanocrystals by doping transition-metal ions. ACS Appl. Mater. Interfaces 5, 9508–9516.

Elzinga, E.J., 2011. Reductive transformation of birnessite by aqueous Mn(II). Environ. Sci. Technol. 45, 6366–6372.

Green, W.J., Stage, B.R., Bratina, B.J., Wagers, S., Preston, A., O'Bryan, K., Shacat, J., Newell, S., 2004. Nickel, copper, zinc and cadmium cycling with manganese in Lake Vanda (Wright Valley, Antarctica). Aquat. Geochem. 10, 303–323.

Greene, A.C., Madgwick, J.C., 1991. Microbial formation of manganese oxides. Appl. Environ. Microbiol. 57, 1114–1120.

Haack, E.A., Warren, L.A., 2003. Biofilm hydrous manganese oxyhydroxides and metal dynamics in acid rock drainage. Environ. Sci. Technol. 37, 4138–4147.

Hem, J.D., 1978. Redox processes at surfaces of manganese oxide and their effects on aqueous metal ions. Chem. Geol. 21, 199–218.

Hens, T., Brugger, J., Cumberland, S.A., Etschmann, B., Frierdich, A.J., 2018. Recrystallization of manganite (γ-MnOOH) and implications for trace element cycling. Environ. Sci. Technol. 52, 1311–1319.

Hirai, S., Yagi, S., Seno, A., Fujioka, M., Ohno, T., Matsuda, T., 2016. Enhancement of the oxygen evolution reaction in Mn^{3+}-based electrocatalysts: correlation between Jahn-Teller distortion and catalytic activity. RSC Adv. 6, 2019–2023.

Hu, C.C., Wu, Y.T., Change, K.H., 2008. Low-temperature hydrothermal synthesis of Mn_3O_4 and MnOOH single crystals: determinant influence of oxidants. Chem. Mater. 2890–2894.

Julien, C.M., Massot, M., Poinsignon, C., 2004. Lattice vibrations of manganese oxides: part I. Periodic structures. Spectrochim. Acta - Part A Mol. Biomol. Spectrosc. 60, 689–700.

Lafferty, B.J., Ginder-vogel, M., Sparks, D.L., Zhu, M., Livi, K.J.T., 2010. Arsenite oxidation by a poorly crystalline manganese oxides. 2. Results from X-ray absorption spectroscopy and X-ray diffraction. Environ. Sci. Technol. 44, 8467–8472.

Lee, S., Xu, H., 2016. XRD and TEM studies on nanophase manganese oxides in freshwater ferromanganese nodules from Green Bay, Lake Michigan. Clay Clay Miner. 64, 523–536.

Lefkowitz, J.P., Elzinga, E.J., 2015. Impacts of aqueous Mn(II) on the sorption of Zn(II) by hexagonal birnessite. Environ. Sci. Technol. 49, 4886–4893.

Lefkowitz, J.P., Elzinga, E.J., 2017. Structural alteration of hexagonal birnessite by aqueous Mn(II): impacts on Ni(II) sorption. Chem. Geol. 466, 524–532.

Lefkowitz, J.P., Rouff, A.A., Elzinga, E.J., 2013. Influence of $_pH$ on the reductive transformation of birnessite by aqueous Mn(II). Environ. Sci. Technol. 47, 10364–10371.

Li, G., Tang, X., Lou, S., Zhou, S., 2014. Large enhancement of ferromagnetism by Cr doping in Mn_3O_4 nanowires. Appl. Phys. Lett. 104, 173105.

Luo, Y., Tan, W., Suib, S.L., Qiu, G., Liu, F., 2018. Dissolution and phase transformation processes of hausmannite in acidic aqueous systems under anoxic conditions. Chem. Geol. 487, 54–62.

Manceau, A., Calas, G., 1986. Nickel-bearing clay minerals: II. Intracrystalline distribution of nickel: an X-ray absorption study. Clay Miner. 21, 341–360.

Manceau, A., Llorca, S., Calas, G., 1987. Crystal chemistry of cobalt and nickel in lithiophorite and asbolane from New Caledonia. Geochim. Cosmochim. Acta 51, 105–113.

Manceau, A., Gorshkov, A., Drits, V., 1992. Structural chemistry of Mn, Fe, Co, and Ni in manganese hydrous oxides: part I. Information from XANES spectroscopy. Am. Mineral. 77, 1133–1143.

Manceau, A., Lanson, M., Geoffroy, N., 2007. Natural speciation of Ni, Zn, Ba, and As in ferromanganese coatings on quartz using X-ray fluorescence, absorption, and diffraction. Geochim. Cosmochim. Acta 71, 95–128.

Manning, B.A., Fendorf, S.E., Bostick, B., 2002. Arsenic(III) oxidation and arsenic(V) adsorption reactions on synthetic birnessite. Environ. Sci. Technol. 36, 976–981.

Maruthapandian, V., Pandiarajan, T., Saraswathy, V., Muralidharan, S., 2016. Oxygen evolution catalytic behaviour of Ni doped Mn_3O_4 in alkaline medium. RSC Adv. 6, 48995–49002.

Maynard, J.B., 2010. The chemistry of manganese ores through time: a signal of increasing diversity of earth-surface environments. Econ. Geol. 105, 535–552.

McKenzie, R.M., 1971. The synthesis of birnessite, cryptomelane, and some other oxides and hydroxides of manganese. Mineral. Mag. 38, 493–502.

McKenzie, R.M., 1972. The sorption of some heavy metals by the lower oxides of manganese. Geoderma 8, 29–35.

Mock, R.P., Schaefer, M.V., Pacheco, J.L., Lake, L., Lee, I., Ying, S.C., 2019. Influence of Fe(II) on arsenic(III) oxidation by birnessite in diffusion-limited systems. ACS Earth Sp. Chem. 3, 550–561.

Murray, J.W., Balistrieri, L.S., Paul, B., 1984. The oxidation state of manganese in marine sediments and ferromanganese nodules. Geochim. Cosmochim. Acta 48, 1237–1247.

Nesbitt, H.W., Canning, G.W., Bancroft, G.M., 1998. XPS study of reductive dissolution of 7Å-birnessite by H_3AsO_3, with constraints on reaction mechanism. Geochim. Cosmochim. Acta 62, 2097–2110.

O'Neill, H.S.C., Navrotsky, A., 1983. Simple spinels: crystallographic parameters, cation radii, lattice energies, and cation distribution. Am. Mineral. 68, 181–194.

Pardee, J.T., 1927. Manganese-bearing Deposits Near Lake Crescent and Humptulips, Washington: Chapter A. Humptulips.

Parikh, S.J., Lafferty, B.J., Sparks, D.L., 2008. An ATR-FTIR spectroscopic approach for measuring rapid kinetics at the mineral/water interface. J. Colloid Interface Sci. 320, 177–185.

Peacock, C.L., Sherman, D.M., 2007. Crystal-chemistry of Ni in marine ferromanganese crusts nodules. Am. Mineral. 92, 1087–1092.

Post, J.E., 1992. Crystal structures of manganese oxide minerals. In: Skinner, H.C.W., Fitzpatrick, R.W. (Eds.), Biomineralization: Processes of Iron and Manganese: Modern and Ancient Environments. Catane Verlag, Cremlingen-Destedt, pp. 51–73.

Post, J.E., 1999. Manganese oxide minerals: crystal structures and economic and environmental significance. Proc. Natl. Acad. Sci. 96, 3447–3454.

Ravel, B., Newville, M., 2005. ATHENA, ARTEMIS, HEPHAESTUS: data analysis for X-ray absorption spectroscopy using IFEFFIT. J. Synchrotron Radiat. 12, 537–541.

Shacat, J.A., Green, W.J., Decarlo, E.H., Newell, S., 2004. The geochemistry of Lake Joyce, McMurdo Dry Valleys, Antarctica. Aquat. Geochem. 10, 325–352.

Shannon, R.D., 1976. Revised effective ionic radii and systematic studies of interatomie distances in halides and chaleogenides. Acta Cryst. A 32, 751–767.

Shumlas, S.L., Singireddy, S., Thenuwara, A.C., Attanayake, N.H., Reeder, R.J., Strongin, D.R., 2016. Oxidation of arsenite to arsenate on birnessite in the presence of light. Geochem. Trans. 17, 1–10.

Silva, G.C., Almeida, F.S., Dantas, M.S.S., Ferreira, A.M., Ciminelli, V.S.T., 2013. Raman and IR spectroscopic investigation of As adsorbed on Mn_3O_4 magnetic composites. Spectrochim. Acta - Part A Mol. Biomol. Spectrosc. 100, 161–165.

Smedley, P.L., Kinniburgh, D.G., 2002. A review of the source, behaviour and distribution of arsenic in natural waters. Appl. Geochem. 17, 517–568.

Song, R., Wang, H.-J., Shou-Hua, F., 2012. Solvothermal preparation of Mn_3O_4 nanoparticles and effect of temperature on particle size. Chem. Res. Chin. Univ. 28, 577–580.

Taylor, R.M., 1968. The association of manganese and cobalt in soils - further observations. J. Soil Sci. 19, 77–80.

Taylor, R.M., McKenzie, R.M., 1966. The association of trace elements with manganese minerals in Australian soils. Soil Res 4, 29–39.

Taylor, R.M., McKenzie, R.M., Norrish, K., 1964. The mineralogy and chemistry of manganese in some Australian soils. Soil Res 2, 235–248.

Tebo, B.M., Johnson, H.A., McCarthy, J.K., Templeton, A.S., 2005. Geomicrobiology of manganese(II) oxidation. Trends Microbiol. 13, 421–428.

Tournassat, C., Charlet, L., Bosbach, D., Manceau, A., 2002. Arsenic(III) oxidation by birnessite and precipitation of manganese(II) arsenate. Environ. Sci. Technol. 36, 493–500.

U.S. EPA, 2007. "Method 3051A (SW-846): Microwave Assisted Acid Digestion of Sediments, Sludges, and Oils", Revision 1. Washington, D.C.

Urusov, V.S., 1983. Interaction of cations on octahedral and tetrahedral sites in simple spinels. Phys. Chem. Miner. 9, 1–5.

Vodyanitskii, Y.N., 2009. Mineralogy and geochemistry of manganese: a review of publications. Eurasian Soil Sci 42, 1170–1178.

Wang, H., Adeleye, A.S., Huang, Y., Li, F., Keller, A.A., 2015. Heteroaggregation of nanoparticles with biocolloids and geocolloids. Adv. Colloid Interf. Sci. 226, 24–36.

Wang, Q., Yang, P., Zhu, M., 2018. Structural transformation of birnessite by fulvic acid under anoxic conditions. Environ. Sci. Technol. 52, 1844–1853.

Wang, Q., Yang, P., Zhu, M., 2019. Effects of metal cations on coupled birnessite structural transformation and natural organic matter adsorption and oxidation. Geochim. Cosmochim. Acta 250, 292–310.

Weaver, R.M., Hochella, M.F., 2003. The reactivity of seven Mn-oxides with $Cr^{3+}_{(aq)}$: a comparative analysis of a complex, aqueous environmentally important redox reaction. Am. Miner. 88, 2016–2027.

Wu, Y., Kukkadapu, R.K., Livi, K.J.T., Xu, W., Li, W., Sparks, D.L., 2018. Iron and arsenic speciation during As(III) oxidation by manganese oxides in the presence of Fe(II): molecular-level characterization using XAFS, Mössbauer, and TEM analysis. ACS Earth Sp. Chem. 2, 256–268.

Wu, Z., Peacock, C.L., Lanson, B., Yin, H., Zheng, L., Chen, Z., Tan, W., Qiu, G., Liu, F., Feng, X., 2019. Transformation of Co-containing birnessite to todorokite: effect of Co on the transformation and implications for Co mobility. Geochim. Cosmochim. Acta 246, 21–40.

Zhao, S., González-Valle, Y.A., Elzinga, E.J., Saad, E.M., Tang, Y., 2018. Effect of Zn(II) coprecipitation on Mn(II)-induced reductive transformation of birnessite. Chem. Geol. 492, 12–19.